Photoluminescence of $Ca_{10}V_6O_{25}$:Eu^{3+}: A theoretical and experimental approach

Mayara M. Teixeira [a],[*],[1],[2], Ivo M. Pinatti [b],[*],[1],[3], José A.S. Laranjeira [c],[4], Guilherme S.L. Fabris [d],[5], Marcio D. Teodoro [e],[6], Ieda L.V. Rosa [a],[7], Alexandre Z. Simões [f],[8], Juan Andrés [g],[9], Julio R. Sambrano [c],[*],[10], Elson Longo [a],[*],[11]

[a] CDMF-UFSCar, Federal University of São Carlos, P.O. Box 676, 13565-905 São Carlos, SP, Brazil
[b] Department of Chemistry, Federal University of Maranhão, Av. Dos Portugueses, 1966, 65080-805 São Luís, MA, Brazil
[c] Modeling and Molecular Simulation Group, São Paulo State University, Bauru, SP, Brazil
[d] Graduate Program in Materials Science and Engineering, Technological Development Center, Universidade Federal de Pelotas, 96010-610 Pelotas, RS, Brazil
[e] Department of Physics, Federal University of São Carlos, Rod. Washington Luiz, Km 235, P. O. Box 676, 13565-905 São Carlos, SP, Brazil
[f] Faculty of Engineering of Guaratinguetá, São Paulo State University (UNESP), 12516-410 Guaratinguetá, SP, Brazil
[g] Department of Analytical and Physical Chemistry, University Jaume I (UJI), Castelló 12071, Spain

ARTICLE INFO

ABSTRACT

$Ca_{10-x}V_6O_{25}$:xEu (x = 0%, 0.5%, 1%, 2%, 4%, and 8%) samples were synthesized by the microwave-assisted hydrothermal method at low temperature and short time. The corresponding structures were investigated by X-ray diffraction with Rietveld refinement, Raman spectra, and field emission scanning electron spectroscopy. Eu^{3+} cations incorporated in $Ca_{10}V_6O_{25}$ provoke a structural disorder with concomitant changes in the morphology. In order to complement and rationalize the structural and electronic effects, computational simulations via density functional theory were employed to rationalize the structural and electronic effects on the constituent clusters of $Ca_{10}V_6O_{25}$ after the Eu^{3+}-doping process. The photoluminescence emission spectra showed characteristic f-f transitions ascribed to Eu^{3+} cations and broadband related to $Ca_{10}V_6O_{25}$. Besides, the matrix-supported a higher percentage of 8% without the quenching effect. These results indicate the potential applications of the obtained materials in optical devices.

1. Introduction

Calcium vanadate, $Ca_{10}V_6O_{25}$ (CaVO) has attracted considerable interest due to its remarkable properties such as superparamagnetic behavior [1], electrochemical sensing [2], and photoluminescence (PL) emissions [3]. Regarding synthesis procedures, CaVO has been obtained by conventional hydrothermal method [1–3], chemical precipitation [4], and recently our research group [5,6] has demonstrated that its synthesis by the microwave-assisted hydrothermal (MAH) method yields samples with high crystallinity [5,6], and exhibits a hexagonal

* Corresponding authors.
  E-mail addresses: mayaramondego@gmail.com (M.M. Teixeira), ivo.pinatti@ufma.br (I.M. Pinatti), jr.sambrano@unesp.br (J.R. Sambrano), elson.liec@gmail.com (E. Longo).
[1] These authors contributed equally to this work.
[2] 0000-0001-9038-0024.
[3] 0000-0002-0964-3075.
[4] 0000-0001-9422-5937.
[5] 0000-0002-0830-5787.
[6] 0000-0002-3557-5555.
[7] 0000-0002-2621-8548.
[8] 0000-0003-2535-2187.
[9] 0000-0003-0232-3957.
[10] 0000-0002-5217-7145.
[11] 0000-0001-8062-7791.

structure with the $P6_3/m$ space group [5].

CaVO presents a band gap energy of around 4 eV with a broadband emission in the visible region when it is excited with ultraviolet light [5]. The bulk lattice of CaVO crystals is composed of three types of distorted six-fold coordination [CaO$_6$] clusters: octahedral, prism and pentagonal pyramidal, and distorted tetrahedral [VO$_4$] clusters that offer possibilities to tune the bond lengths, defects, and vacancies [5]. Its PL emission arises due to the structural order-disorder effect that forms localized states in the forbidden band gap and gives rise to tunable distortion in the VO$_4$ tetrahedral, eventually enabling intrinsic light emission associated with $^3T_2 \rightarrow {}^1A_1$ and $^3T_1 \rightarrow {}^1A_1$ transitions [5].

Rare-earth doped complex inorganic materials have attracted researchers as they exhibit a wide range of applications in the field of display systems, solid-state laser, thermometry, optoelectronic devices, optical fibers, scintillators, owing to their robust 4f–5d transitions [7–9]. Among them, trivalent europium cations (Eu^{3+}) present characteristic PL emission spectra with typical $^5D_0 \rightarrow {}^7F_J$ ($J = 0, 1, 2, 3, 4$) transitions, being the most intense PL red emission at around 615 nm ($^5D_0 \rightarrow {}^7F_2$), while the host lattice needs to display thermal stability and durability. Several works published by our group related the incorporation of Eu^{3+} cations in different matrices for PL application such as Ag$_2$WO$_4$ [10,11], β-Ag$_2$MoO$_4$ [12], CaZrO$_3$ [13], CaMoO$_4$ [14], CaWO$_4$ [15,16], CeO$_2$ [17], Zn$_2$TiO$_4$ [18], ZrO$_2$ [19], SrTiO$_3$ [20], CaTiO$_3$ [21,22], ZnS [23], In(OH)$_3$ [24], Ca$_{10}$(PO$_4$)$_6$(OH)$_2$ [25], SrWO$_4$ [26], SrMoO$_4$ [27], BaMoO$_4$ [28], Y$_2$O$_3$ [29], and SrBi$_2$Nb$_2$O$_9$ [30]. Moreover, it was observed that the PL emissions of Eu^{3+} cations can be well-sensitized in other calcium vanadate matrixes of different structures such as Ca$_3$(VO$_4$)$_2$ and Ca$_2$V$_2$O$_7$ [7,31].

Inspired by the above considerations and unique characteristics, such as cost-effective, stability, and environmentally friendly, CaVO can be considered a promising host material of rare earth cations. Here, we report a novel study on incorporating Eu^{3+} cations at the CaVO lattice (CaVO:xEu (x = 0%, 0.5%, 1%, 2%, 4%, and 8%) obtained by the MAH method. Different amounts of Eu^{3+} cations are responsible for structural and morphological changes observed along with distinct PL emissions intensities. In addition, density functional theory (DFT) simulations have been carried out to complement the experimental results on the structure, electronic properties, and Raman vibrational modes.

2. Experimental

2.1. Synthesis

The CaVO:xEu (x = 0%, 0.5%, 1%, 2%, 4%, and 8%) samples were synthesized by the MAH method previously described by our research group [5]. Briefly, NH$_4$VO$_3$ (0.2363 g) was dissolved in 35 mL of distilled water at 50 °C, and stoichiometric amounts of CaCl$_2$.2H$_2$O were dissolved in 35 mL of distilled water at room temperature. Eu(NO$_3$)$_3$ solution was prepared with the dissolution of Eu$_2$O$_3$ powder (pre-calcined at 900 °C for 2 h) in a hot aqueous solution of dilute HNO$_3$. Excess nitric acid was evaporated, and the solution was completed with distilled water (0.1 M). Then, for the pure CaVO sample, only Ca^{2+} and VO$_4^{3-}$ solutions were mixed. For Eu-samples, stoichiometric amounts of the Ca^{2+} and Eu^{3+} solutions (0.5%, 1%, 2%, 4%, and 8% mass fractions) were added to the VO$_4^{3-}$ solution, and the pH of all samples was adjusted to 12.5 using a 6.0 mol.L^{-1} of KOH solution. After that, the suspensions were transferred to the MAH system at 120 °C for 32 min. Finally, the precipitates formed were collected, washed with distilled water, and dried in a conventional furnace at 60 °C for 12 h.

2.2. Characterizations

X-ray diffraction (XRD) pattern was performed on a diffractometer Rigaku, DMax/2500PC with Cu Kα radiation (λ = 1.5406 Å) collected in the 2θ from 5° to 75° operating at 40 kV and 50 mA. Rietveld refinements were performed in the 2θ range from 5° to 110° using the general structure analysis (GSAS) program. The morphology was observed using a field-emission scanning electron microscopy (FE-SEM) Supra 35-VP Carl Zeiss operated at 15 kV. The structure was analyzed by Raman spectra with a Horiba Jobin-Yvon (T64000) spectrometer coupled to a CCD detector with a 514 nm line of an argon ion laser. The spectra were collected in the range of 100—1000 cm^{-1}. The UV–visible diffuse reflectance spectra (UV–vis DRS) were obtained with a Varian (Cary 5 G) spectrophotometer in the range of 250—800 nm operated in a diffuse reflectance mode. Photoluminescence measurements at room temperature were performed using the excitation source Cobol-Zouk at 355 nm laser-focused on a 200 μm spot with an incident power of ~5 mW. The luminescence signal was dispersed by a 50 cm spectrometer (Andor/Shamrock) and detected by a Silicon Charged Coupled Device (Andor/Idus BU2). The emission and excitation spectra were carried out at room temperature on a Horiba Jobin-Yvon Spex Triax 550 Fluorolog 3 spectrofluorometer equipped with a 450-W continuous xenon lamp. The detection was performed with a Hamamatsu R928P photomultiplier.

2.3. Computational method and model system

The computational simulations were performed under the periodic density functional theory (DFT) approach using the CRYSTAL17 software [32], alongside the use of B3LYP hybrid functional and a combination of all-electron and pseudo-potentials basis sets. The calcium, vanadium, oxygen, and trivalent europium (Eu^{3+}) atomic centers were described by 86–511d3G [33], 86–411d4G [34], 6–31d1 [35], and ECP52MWB (http://www.theochem.unistuttgart.de/pseudopotentials) basis set [36,37], respectively. The B3LYP functional and the atomic centers of Ca, V, and O were adopted as a continuity of previous work [5].

The systems analyzed were certified as a minimum by diagonalizing the Hessian matrix concerning lattice parameters and atomic positions and then analyzing the vibrational modes at the Γ point. The optimization convergence criteria for the gradient components and nuclear displacements were set with tolerances on their root mean square set to 3×10^{-5} and 1.2×10^{-4} a.u., respectively. The precision in the calculation of the infinite Coulomb and Hartree-Fock exchange series was controlled by five thresholds α_i, with i = 1–5, so that the contributions of two-electron interactions are neglected when the overlap between atomic functions is below $10^{-\alpha_i}$; and in this work, these parameters have been set to 8, 8, 8, 8, and 16, and the Pack-Monkhorst and Gilat nets were set to 4. The Raman intensities were obtained using the coupled perturbed Hartree-Fock/Kohn-Sham approach [38]. The electronic structure (band structure and density of states) was determined using the same k-point sampling employed for the diagonalization of the Fock matrix in the optimization process.

The Eu^{3+} incorporation in the CaVO matrix was simulated by the substitution of one Ca^{2+} cation for one Eu^{3+} cation in a unit cell with 41 atoms, without vacancies and charges compensation, since it was modeled as a perfect crystal, free of defects and vacancies, which permits a qualitative comparison with the experimental data. It is worth noting that the europium pseudopotential basis set was parametrized to represent the Eu^{3+} cation (http://www.theochem.unistuttgart.de/pseudopotentials). In addition, the experimental refinement of structural parameters was used as a starting point for the simulations.

The distortion index I is defined based on the bond length and can be calculated using the following equation:

$$I = \frac{1}{n} \sum_{i=1}^{n} \frac{|l_i - l_{avg}|}{l_{avg}},$$

where l_i is the distance between the central atom and the neigbour atoms, belonging to the local coordination, and l_{avg} is the average bond length, and n is the number of atoms in the cluster.

3. Results and discussion

3.1. XRD patterns

Fig. 1 shows the CaVO:*x*Eu (*x* = 0%, 0.5%, 1%, 2%, 4%, and 8%) XRD patterns. The diffractograms show that the samples correspond to the hexagonal $Ca_{10}V_6O_{25}$ structure that belongs to the *P63/m* space group (JCPDS No. 52-649). No additional diffraction peaks referring to the secondary phase were observed, indicating that Eu^{3+} cations were efficiently introduced into the CaVO host lattice.

Structural refinement data for CaVO:*x*Eu (*x* = 0%, 0.5%, 1%, 2%, and 4%) samples and simulations confirmed the hexagonal structure (see Table S1 and Fig. S1). The low deviations of the statistical parameters (R_{wp}, R_p, χ^2, and R_{Bragg}) show the reliability of the Rietveld refinements. An analysis of the results renders that as the amount of Eu^{3+} increased, the cell volume gradually expanded due to the effective Eu^{3+} cations substitution into the CaVO matrix.

The replacement of Ca^{2+} divalent cations by Eu^{3+} trivalent cations may cause a relaxation in the CaVO host lattice because for each two Eu^{3+} cations replacing three Ca^{2+} cations, therefore, there is the formation of a calcium vacancy (V_{Ca}) in the lattice, where Eu^{3+}_{Ca} is the Eu^{3+} cations substituted Ca^{2+} sites. (Eq. 1):

$$3Ca^{2+} + 2Eu^{3+} \rightarrow 2Eu^{3+}_{Ca} + 1\ V_{Ca} \qquad (1)$$

The increased proportion of Eu^{3+} in the CaVO host lattice causes an increase in V_{Ca} numbers, which distorts the lattice, and new cluster arrangements are formed in the unit cell of the CaVO matrix. Thus, there were observed some differences in the lattice constants for the doped samples (Table S1) that were confirmed by the peak intensities, peak width, and peak positions of the (211) and (300) plans in the diffractograms (Fig. S2).

The unit cell of the $Ca_{10}V_6O_{25}$ comprises network-forming [VO_4] clusters and network-modifying [CaO_6] clusters coordinated by six oxygen atoms with prism, octahedral, and pentagonal pyramidal symmetry [5]. It is important to emphasize that the Eu insertion site was chosen after a careful investigation of the preferential substitution in three different clusters ([CaO_8], [CaO_7], and [CaO_5]), in which it was found that the [CaO_8] is the most favorable site for the Eu^{3+} substitution.

Fig. 2 displays the constituents cluster of CaVO after Eu^{3+} incorporation while the average bond length (L) and the relative distortion index (I), as a measure of the local structural organization (I<0) or distortion (I>0), are highlighted.

The Eu^{3+} cations insertion leads to the reorganization of the CaVO network with the formation of new [EuO_8], [CaO_7], and [CaO_5] clusters, eliminating almost all [CaO_6] clusters found in the pristine CaVO structure. Through the Eu-substitution process, it was identified that the average bond lengths of the [EuO_8] cluster decrease if compared to the [CaO_8] cluster of the pure CaVO matrix, along with a decrease of the distortion in the closest [VO_4] cluster, indicated by the I< 0. However, the presence of the Eu^{3+} cations leads a short, medium, and long-range distortion that propagates in the [VO_4], [CaO_7], and [CaO_5] clusters, which causes a small expansion of ~0.18% in the lattice parameters. This result is confirmed by a small expansion in the volume of the experimental samples by the Rietveld refinement (Table S1). Therefore, a deviation from Vegard's law was observed when occur replacement of Ca^{2+} divalent cations, ionic radii 1.12 Å, by Eu^{3+} trivalent cations, ionic radii 1.066 Å, in CaVO matrix.

3.2. Morphological analysis

Fig. 3 shows the FE-SEM images of the CaVO:*x*Eu particles. The CaVO matrix has a bundle-like morphology with medium-width stems of 508 ± 141 nm (Fig. 3a). With the insertion of 0.5% of Eu^{3+}, there is a decrease in the medium width of the stems to 225 ± 55 nm, and it was also observed that the particles are less aggregated (Fig. 3b).

The image of the particles with 1% of Eu^{3+} cations shows a greater separation of the nanostems with a medium width of 272 ± 82 nm, and some nanostems convert to nanowires (Fig. 3c). Also, it can be seen that the concentration of Eu^{3+} cations changes the surface energy, shape, and size of the particles and thus decreases the interaction of the stems.

The sample with 2% of Eu^{3+} cations illustrates a bundle-like morphology with a medium width of 358 ± 93 nm (Fig. 3d). On the other hand, with higher concentrations of 4% and 8% Eu^{3+} (Fig. 3e and f), there is a change in morphology, and some nanostems convert to nanospheres altogether with bundle-like morphology. With 4% and 8% Eu^{3+} cations, the samples did not show homogeneity in morphology and particle size. Therefore, it can be concluded that Eu^{3+} ions cause a structural disorder that alters the symmetry of the network-modifying [CaO_6] clusters and network-forming [VO_4] clusters of the matrix. The intercluster (intermediary range) and intracluster (local range) interactions by orientation, induction, and dispersion forces propagate disorder throughout the crystal network [39,40]. Thus, new cluster arrangements are formed and change the energy of the exposed surfaces and the interaction between particles, and as a result, there is an alteration in the final morphology.
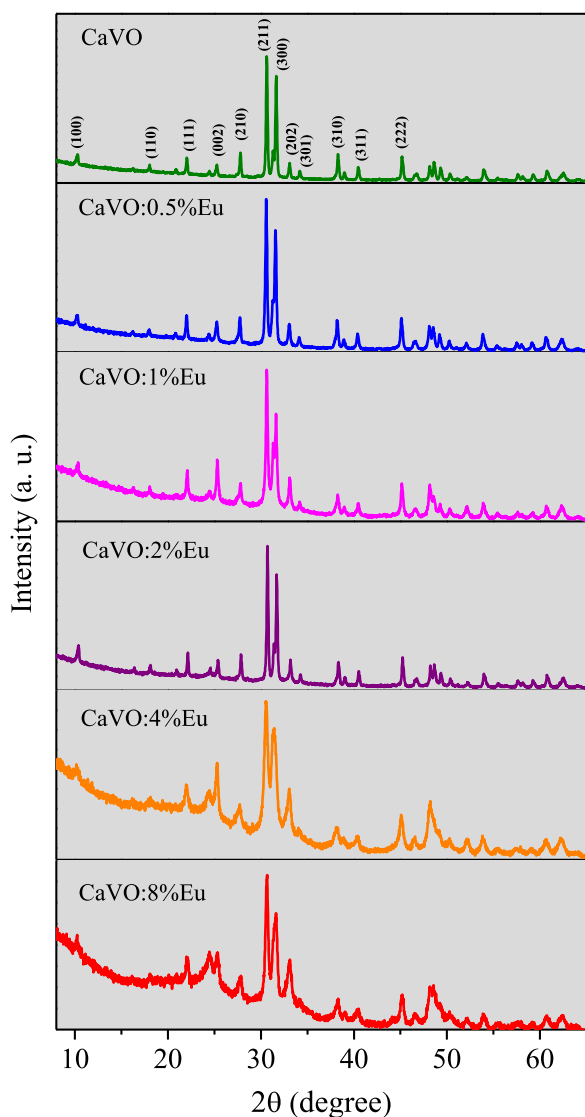

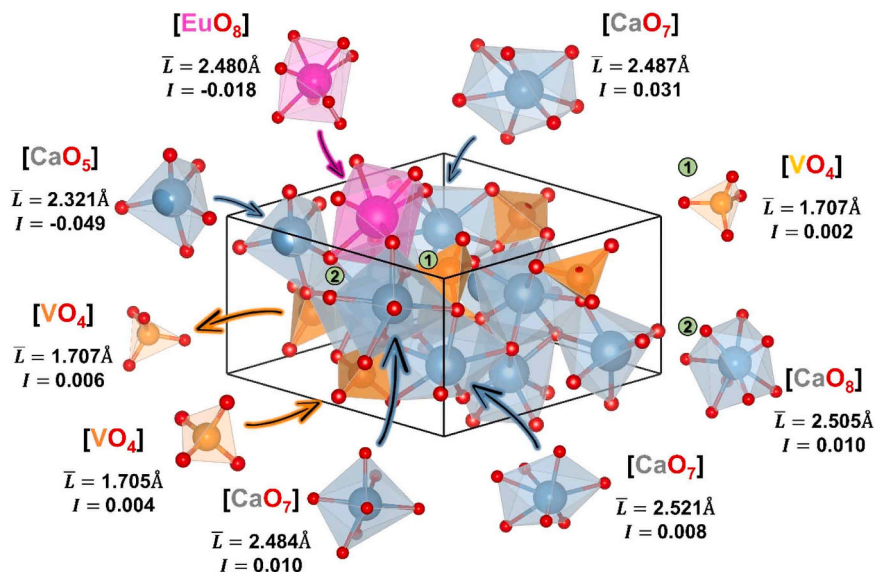**Fig. 1.** XRD patterns of the CaVO:xEu (x = 0%, 0.5%, 1%, 2%, 4%, and 8%) samples.

Fig. 2. A polyhedral representation of all clusters for $Ca_{10}V_6O_{25}$ with the incorporation of Eu^{3+} cation, including the average bond length ($\bar{L}$) and I. Calcium, vanadium, oxygen, and europium ions are represented by gray, orange, red, and magenta colors, respectively.

3.3. Raman spectroscopy

Fig. 4 presents the Raman spectra for all the samples and the spectra obtained by computational simulations. For the CaVO matrix, 63 active Raman modes are theoretically expected according to the irreducible representation:

$$\Gamma = 24A_g^{'} + 24E_g^{'} + 15E_g^{'}$$

All the theoretical Raman frequencies of the CaVO and CaVO:10%Eu samples are presented in Table S2. Nine experimental active Raman modes were observed for the CaVO:xEu samples, as shown in Fig. 4a. The intense band at 356 cm^{-1} is related to the A_g mode of bending vibration of the O−V−O bond of ν_3 [5]. The modes at 393 and 406 cm^{-1} are associated with the A_g bending vibration of the O−V−O bond of ν_4 [5]. The mode at 814 cm^{-1} can be attributed to the E_{2g} antisymmetric stretching of the VO_4 of ν_3 [5]. Finally, the modes at 839 and 878 cm^{-1} are ascribed to the A_g symmetrical stretching vibration of the V−O bond of ν_1 [5]. Fig. 4b shows a magnification of lower frequency region, and lower intensities modes at 130, 207, and 241 cm^{-1}, which are related to the lattice modes of $[CaO_x]$ clusters could be seen. All these experimental modes meet with the theoretical ones and agree with the literature [5,41].

Also, a small blue shift for the Eu-samples modes was observed and compared to the CaVO sample (Fig. 4c). The displacement to lower vibrational frequency is related to the increase in the V-O bond lengths [42,43] of the stretching mode in the $[VO_4]$ clusters after the substitution process of Ca^{2+} by Eu^{3+} to render the $[EuO_8]$ clusters and V_{Ca} vacancies, as it is observed in other Eu^{3+} doped calcium vanadate phases [44].

The peaks theoretical Raman spectra have a similar trend as observed for pure CaVO, and a small frequency shift of 8% to higher frequencies. For the CaVO:10%Eu (theoretical), experimental and theoretical Raman bands agree for high frequencies, and the shape and peaks have a similar pattern. However, for lower frequencies, the peaks could not be visually identified since they appear distributed in smaller peaks (see Table S2 in the supplementary material). The small frequency shift for the pure CaVO and the dilution of the lower frequency peaks on the CaVO:10%Eu (theoretical) sample can be associated with the distortion effect in the network, caused by the symmetry breaking and change in the short-range order.

3.4. Optical properties

The optical band gap energy (E_{gap}) of the CaVO:xEu (x = 0%, 0.5%, 1%, 2%, 4%, and 8%) samples and energy levels formed in the medium range were calculated employing UV–vis DRS. Fig. S3 shows that all samples showed absorption at 350 nm in the ultraviolet region. The electronic transition was considered as direct allowed [5], and using Kubelka-Munk and Wood-Tauc equation [45,46], the calculated E_{gap} = 4.00 eV for the CaVO is in agreement with the $Ca_{10}V_6O_{25}$ structure reported [5,6]. The Wood-Tauc theory shows that an ordered structure in the medium-range has a sharp vertical curve. The increase in Eu^{3+} proportion makes the UV–vis DRS curve more sloped, with lower E_{gap} values of 3.65 eV and 3.64 eV for the CaVO:4%Eu and CaVO:8%Eu, respectively, indicating a higher concentration of defects density (new states) in the medium range due to inclination of the Urbach tail [46,47]. These defects can be associated with increased V—O and Ca—O bond lengths. The distortion of the corresponding clusters is propagated from the short to medium and long-range in the crystal lattice, as can be observed by XRD, values of the Rietveld refinement, Raman, and UV–vis DRS spectra.

The band structure of CaVO and CaVO:10%Eu samples were theoretically calculated and shown in Fig. 5a and b, respectively. The band gap energy values of the CaVO and CaVO:10%Eu samples are 3.29 eV and 3.07 eV, respectively. These values are slightly lower than those experimentally obtained but present the same tendency as the experimental data. In the CaVO:10%Eu sample, the Eu-substitution process seems to change the inner bands, showing increased occupied zone concentration. Also, there is a change in the form of the bands, especially in the first unoccupied one, which shows a less flat behavior, indicating an increase in electron mobility and, consequently, enhancing the electronic transfer process.

Fig. 5c depicts the density of states of the CaVO model. An analysis of the results points out that the maximum VB is composed mostly of oxygen contribution with a small contribution of calcium atoms. In contrast, the CB minimum is mostly composed of vanadium atoms with a smaller presence of oxygen. In the CaVO:10%Eu (Fig. 5d), the major contribution of the vanadium atoms to the CB is observed. In contrast, europium states have higher contributions for VB. The band gap energy decrease can be associated with forming $[CaO_7]$ and $[CaO_5]$ clusters with different electronic densities. This electronic effect induces the appearance of localized excited states due to the variation of the
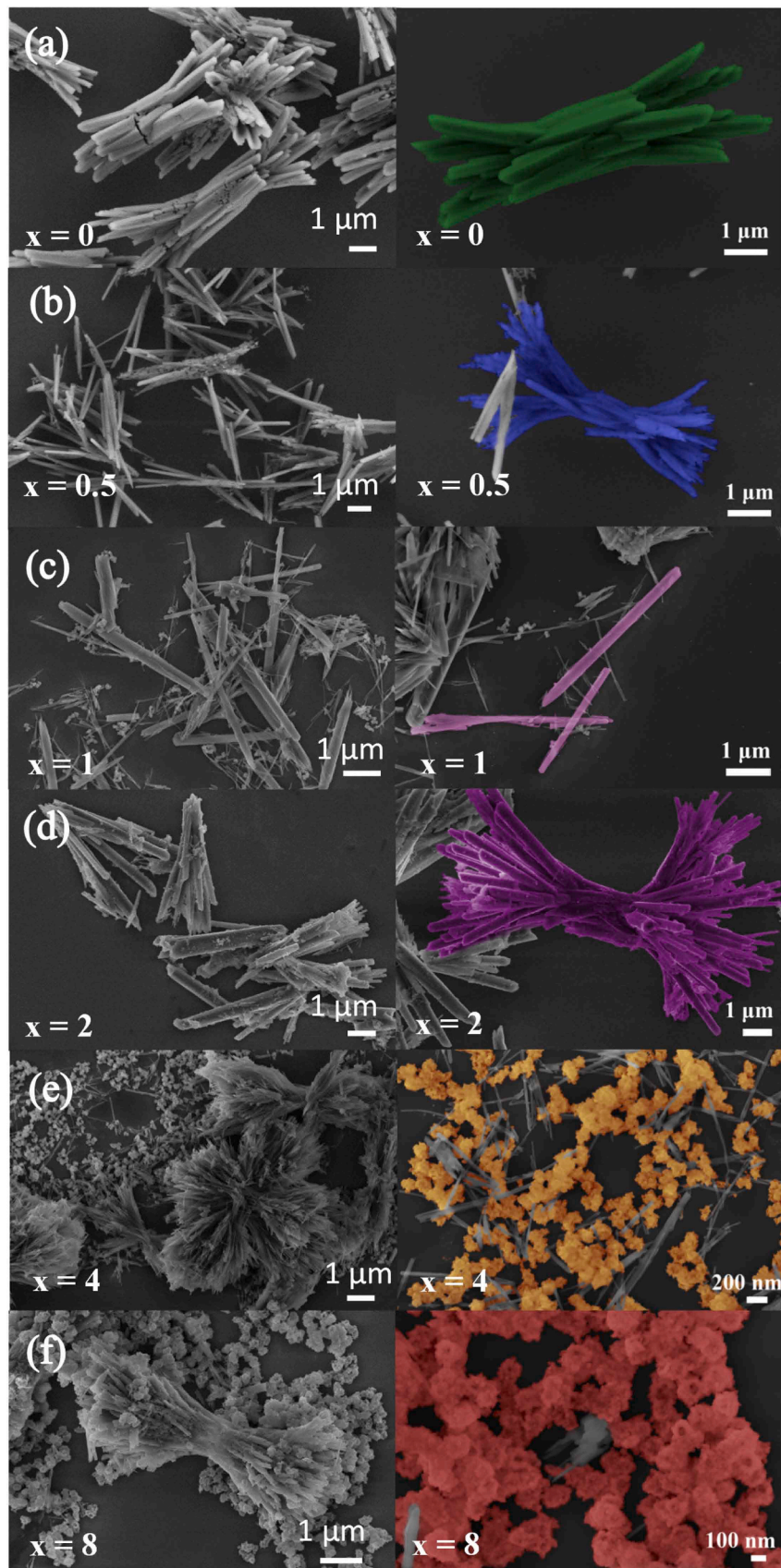
Fig. 3. FE-SEM images of CaVO:xEu: (a) x = 0, (b) x = 0.5%, (c) x = 1%, (d) x = 2%, (e) x = 4%, and (f) x = 8%.

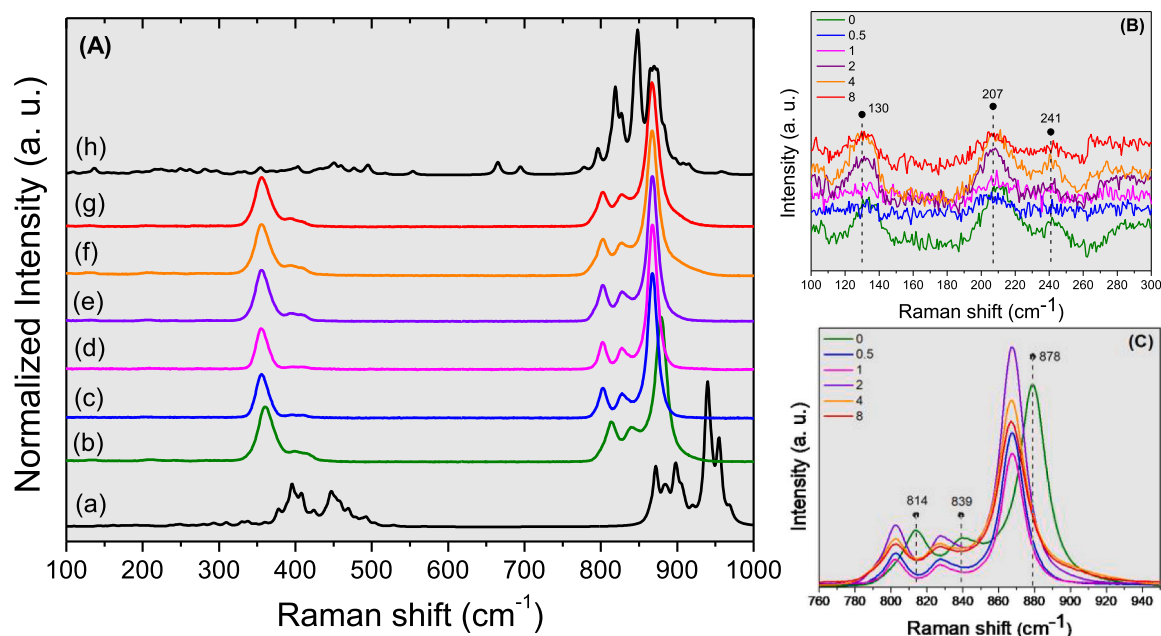**Fig. 4.** . (A) Raman spectra of the CaVO:*x*Eu (*x* = 0%, 0.5%, 1%, 2%, 4%, and 8%) samples; (B) Magnification of the low-frequency region; (C) Magnification of the high-frequency region. The samples were labeled as: (a) CaVO x = 0 (theoretical), (b) CaVO, (c) CaVO:*0.5%*Eu, (d) CaVO:*1%*Eu, (e) CaVO:*2%*Eu, (f) CaVO:*4%*Eu, (g) CaVO:*8%*Eu, (h) CaVO:10%Eu x = 10 (theoretical).
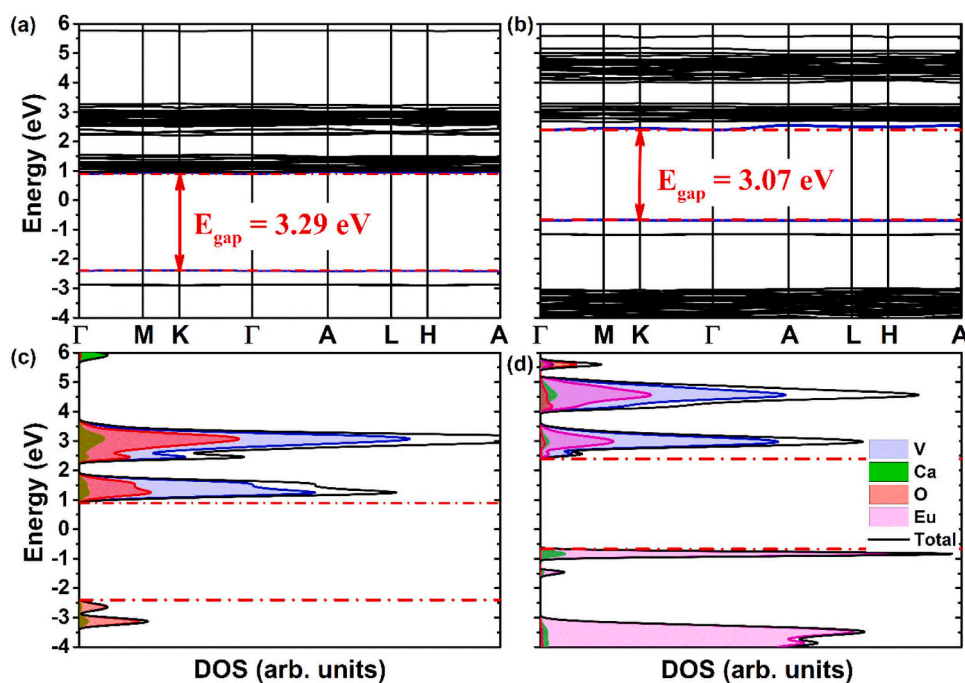
Fig. 5. . (a), (c) Band structure and density of states of CaVO, and (b), (d) CaVO:10%Eu.

structural order/disorder in the crystalline lattice.

The electron density of the pristine CaVO (Fig. 6a) and CaVO:10%Eu (Fig. 6b) reveal that the presence of the Eu cations increases the potential of the closer Ca atoms and decreases its site. Also, the highest occupied crystalline orbital (HOCO) and lowest unoccupied crystalline orbital (LUCO) of the pristine and doped systems were plotted, as shown in Fig. 6c.

The comparative analysis of the HOCO and LUCO indicated that the Eu-substitution provokes a major change in the HOCO that can be associated with the creation of new states, as can be seen in Fig. 6c,

causing a more concentrated orbital localization over the structure. An animation video of the HOCO and LUCO can be found in the supplementary material.

Supplementary material related to this article can be found online at doi:10.1016/j.jallcom.2024.173525.

The Mülliken population analysis of the [CaO$_8$] and [EuO$_8$] clusters indicates that the Eu-substitution increases the bonding population from 29 to 84 m|e| and the charge transfer around the substituted site. Also, it is important to observe that the choice of this approach was arbitrary because when comparing different systems, the presence (or absence) of
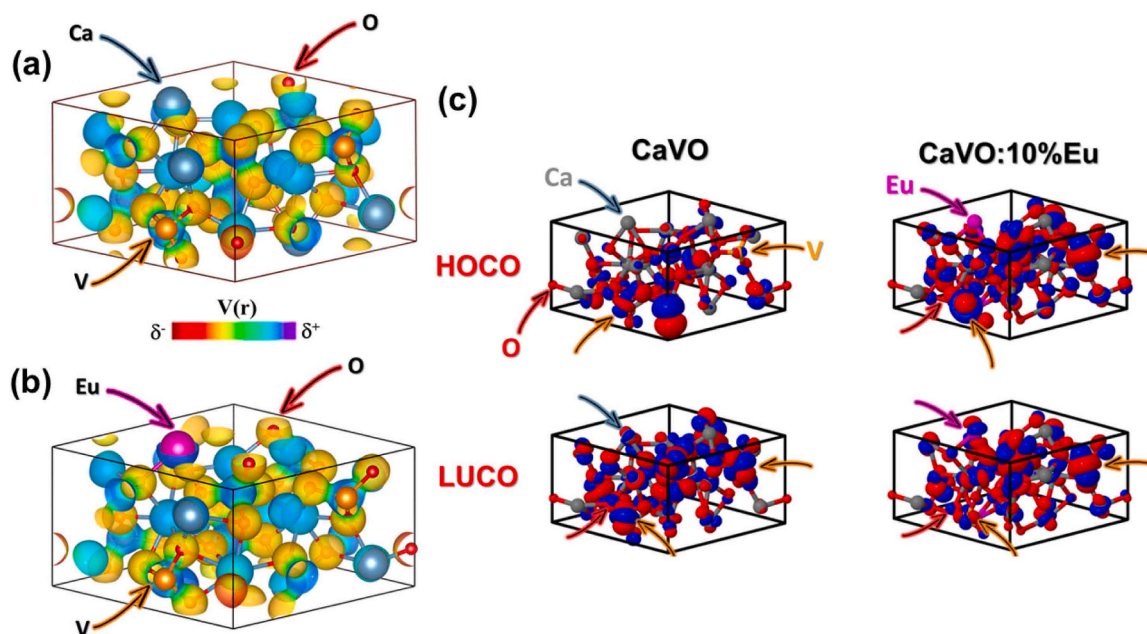
Fig. 6. Electron density of (a) CaVO and (b) CaVO:10%Eu-sample, (c) Highest Occupied Crystalline Orbital (HOCO) and Lowest Unoccupied Crystalline Orbital (LUCO) of both structures, respectively.

defects will affect both systems equally.

3.5. Photoluminescence properties

Fig. 7 shows the room temperature PL emission spectra (λ_{ex} = 355 nm) of the CaVO:xEu (x = 0%, 0.5%, 1%, 2%, 4%, and 8%) samples. The CaVO matrix shows a broadband PL emission from 400 to 750 nm with a maximum centered around 560 nm (inset of Fig. 7a). This band can be associated with the charge transfer (CT) process between CB composed of V orbitals hybridized with O orbitals of VB and a small content of Ca orbitals [5]. The PL emission band deconvolution resulted in two sub-bands centered at 535 nm (green emission) and 618 nm (orange emission) (see Fig. S4). The deconvoluted *Em1* band corresponds to the $^3T_2 \rightarrow {}^1A_1$ electronic transition, whereas the *Em2* band is attributed to the $^3T_1 \rightarrow {}^1A_1$ electronic transition (see Fig. 7c) [6]. Moreover, the PL emission spectra of Eu-samples present Eu^{3+} peaks due to transitions of the $^5D_0$ excited state to ^7F_J (J = 1, 2, 3, and 4) ground state at 593, 614, 650, and 698 nm, respectively. Additionally, it was observed low-intensity peaks centered at 538 and 558 nm regarding $^5D_1 \rightarrow {}^7F_1$ and $^5D_1 \rightarrow {}^7F_2$ transitions, respectively. All Eu-samples showed a maximum emission intensity at 614 nm corresponding to the $^5D_0 \rightarrow {}^7F_2$ transition [31].

The CaVO:0.5%Eu sample showed an increase in the emission of the CaVO matrix; see inset of Fig. 7a. The Ca^{2+}-by-Eu^{3+} substitution forms V_{Ca} that promotes the formation of intermediate levels within the forbidden region and thus increases the emission of the matrix. In higher Eu^{3+} concentrations (x = 1%, 2%, 4%, and 8%), there is a decrease in the emission intensity of the [VO$_4$] clusters since the electrons are transferred to the Eu^{3+} cations due to the greater contribution of the Eu states in both CB and VB. The high intensity of Eu^{3+} emission shows that CaVO is an efficient host matrix that enhanced the emission of rare earth even for the highest percentage of 8% mass fraction, and the quenching effect was not observed (Fig. 7b), as observed in other matrices [10,22, 27,28,48–53].

A schematic CT mechanism between the CaVO matrix and Eu^{3+} ions has been proposed (Fig. 7c) [50,54]. It is known that the CaVO matrix can be excited from the $^1A_1$ ground state to the $^1T_2$ and $^1T_1$ excited states. Then, there is an interstate transition to the $^3T_2$ and $^3T_1$ excited states of lower energy after a decay with photon emission to the $^1A_1$

state. With the insertion of Eu^{3+} cations, there is a CT between the states of the CaVO matrix to Eu^{3+} cations, and a radiative decay occurs [54]. The CIE chromaticity coordinate values show the emission colors of the samples (Fig. 7d) are located in CaVO (x = 0.47, y = 0.42), CaVO:*0.5%* Eu^{3+} (x = 0.47, y = 0.43), CaVO:*1%*Eu^{3+} (x = 0.62, y = 0.35), CaVO:*2%*Eu^{3+} (x = 0.64, y = 0.33), CaVO:*4%*Eu^{3+} (x = 0.65, y = 0.33), and CaVO:*8%*Eu^{3+} (x = 0.65, y = 0.33). The (x, y) coordinate values show that when samples were excited at 355 nm, the CaVO matrix has yellow color emission, and with the substitution of Ca^{2+}-by-Eu^{3+} cations, the color displaced from yellow to red.

Fig. 8 shows the excitation spectra in the 250—500 nm range, monitoring the emission at 613 nm, ascribed to the more intense $^5D_0 \rightarrow {}^7F_2$ transition of Eu^{3+}. It was possible to observe a broad PL emission band between 250 and 375 nm centered at 280 nm due to the CT process. This band has contributions from O^{2-}-Eu^{3+} (around 280 nm) and O^{2-}-V^{5+} (around 300 nm) transitions [55,56]. Additionally, it was observed in longer wavelength region, three main Eu^{3+} f-f transitions, located at 394, 415, and 464 nm, referred to as $^7F_0 \rightarrow {}^5L_6$, $^7F_0 \rightarrow {}^5D_3$ and $^7F_0 \rightarrow {}^7D_2$ transitions, respectively [49].

Fig. 9a shows the PL emission spectra of CaVO:xEu (x = 0.5%, 1%, 2%, 4%, and 8%) samples excited at 330 nm. These spectra present four main Eu^{3+} f-f transitions centered at 592, 616, 649, and 700 nm, ascribed to the $^5D_0 \rightarrow {}^7F_J$ (J = 1–4) transitions, respectively. The samples also present lower intensity peaks at 535 nm and 579 nm, ascribed to the $^5D_1 \rightarrow {}^7F_1$ and $^5D_0 \rightarrow {}^7F_0$ transitions, respectively [50]. The PL emission spectra in the range of 500–750 nm excited at 394 nm related to the $^7F_0 \rightarrow {}^5L_6$ transition of Eu^{3+} are shown in Fig. 9b. The samples present the same Eu^{3+} f-f transitions when excited at 330 nm, implying that these samples can be good phosphors when excited both in the short or long UV region [10,11].

The $^5D_0 \rightarrow {}^7F_2$ and $^5D_0 \rightarrow {}^7F_4$ transitions are mainly governed by electric dipole (ED) mechanisms, the former sensitive to local environmental factors such as symmetry and the local field of the Eu^{3+} cations. On the other hand, $^5D_0 \rightarrow {}^7F_1$ transition is governed by magnetic dipole (MD) mechanism. Generally, the intensity ratio of ED and MD transitions gives information about the local symmetry of Eu^{3+} cations in the host matrix, and increasing values mean a more asymmetric nature. It was observed that greater intensity of the $^5D_0 \rightarrow {}^7F_2$ ED transition for all samples irrespective of the $^5D_0 \rightarrow {}^7F_1$ MD one, indicating that Eu^{3+}
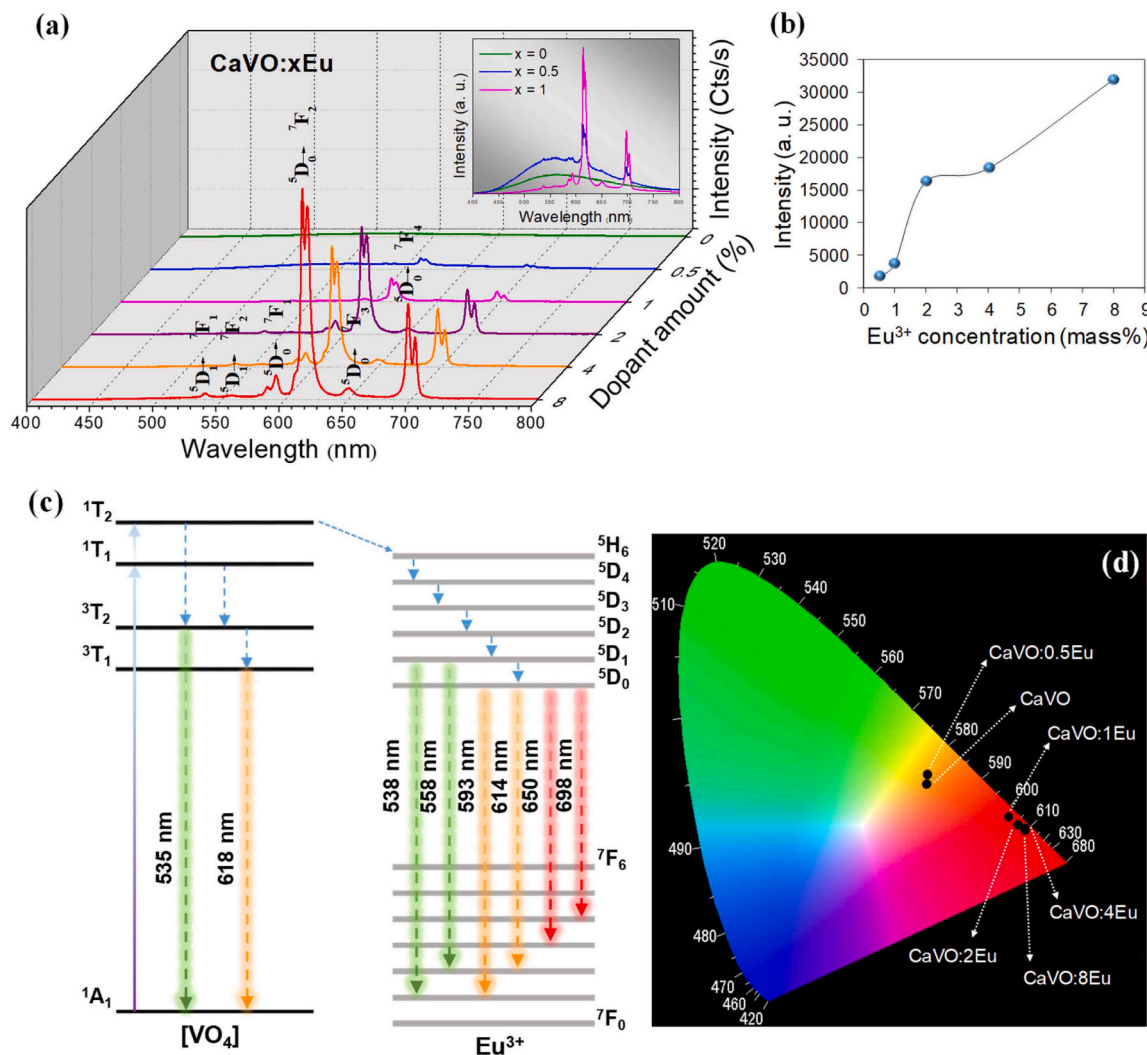
Fig. 7. (a) PL emission spectra of the CaVO:xEu (x = 0%, 0.5%, 1%, 2%, 4%, and 8%) excited at 355 nm. Inset: emission spectra of the CaVO:xEu (x = 0%, 0.5%, and 1%) samples; (b) The dependence of Eu^{3+} mass fraction on the emission intensity (613 nm); (c) The schematic diagram of electron transition of [VO$_4$] cluster to Eu^{3+} cations; (d) CIE diagram.
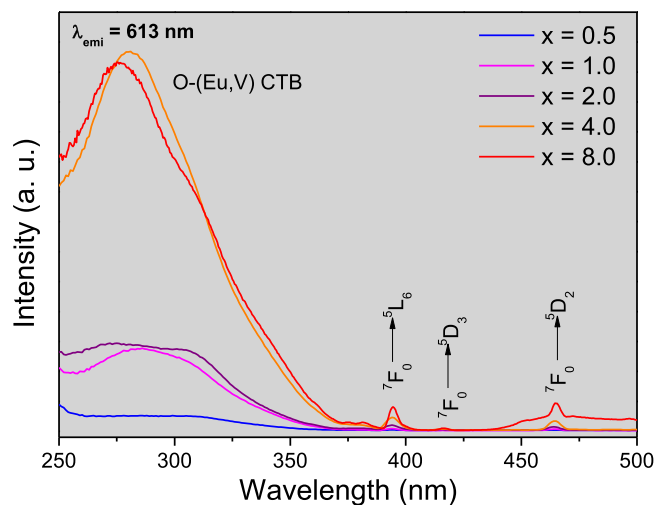

Fig. 8. PL excitation spectra of the CaVO:xEu (x = 0.5%, 1%, 2%, 4%, and 8%) samples monitoring the emission at 613 nm.

cations are located at the site of non-inversion symmetry, this was also observed through the theoretical calculations.

4. Conclusion

In this work, CaVO:xEu samples were efficiently synthesized by the microwave-assisted hydrothermal method. The Eu-substitution increases the distortion in the network-forming [VO$_4$] clusters and network-modifying [CaO$_6$] clusters and new clusters are formed in the unit cell: [EuO$_8$], [CaO$_7$], and [CaO$_5$] as identified by DFT simulations. The Eu^{3+} incorporation expands the cell volume and introduces new localized electronic states with a concomitant decrease in the E_{gap} value. The FE-SEM images show that the concentration of Eu^{3+} cations strongly influences particle morphology and size. The PL emissions render that the CaVO matrix was an efficient host for Eu^{3+} cations, and no quenching effect was observed up to the limit of 8%. All Eu-samples present the characteristic PL emission peaks of Eu^{3+} cations, with the most intense transition at 614 nm ($^5D_0 \rightarrow {}^7F_2$). The CIE chromaticity diagram shows that the increase in substitution favored the emission displacement towards the red region characteristic of the Eu^{3+} cations.
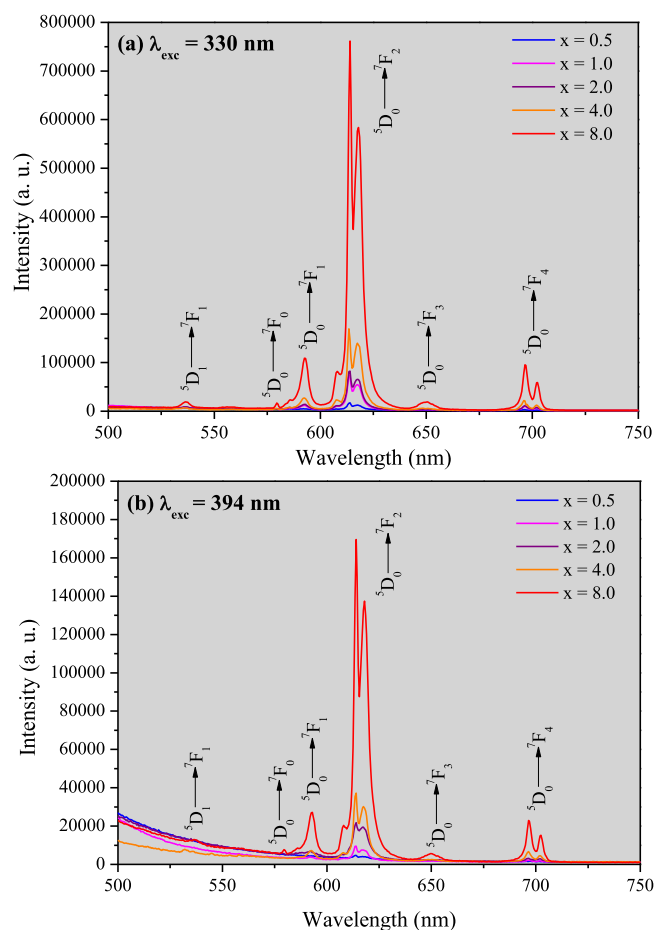
Fig. 9. PL emission spectra of the CaVO:xEu (x = 0.5%, 1%, 2%, 4%, and 8%) samples excited at (a) 330 nm and (b) 394 nm.

CRediT authorship contribution statement

Fabris Guilherme S. L.: Writing – original draft, Methodology, Investigation, Formal analysis. **Teodoro Marcio D.:** Writing – original draft, Visualization, Formal analysis. **Pinatti Ivo M.:** Writing – original draft, Visualization, Methodology, Investigation, Formal analysis, Conceptualization. **Laranjeira José A. S.:** Methodology, Investigation, Formal analysis. **Teixeira Mayara Mondego:** Writing – original draft, Visualization, Methodology, Investigation, Formal analysis, Conceptualization. **Sambrano Julio R.:** Writing – review & editing, Writing – original draft, Visualization, Supervision, Resources, Methodology, Formal analysis. **Longo Elson:** Writing – review & editing, Visualization, Supervision, Resources, Project administration, Methodology, Funding acquisition, Formal analysis, Data curation, Conceptualization. **Simões Alexandre Z.:** Writing – original draft, Visualization, Resources, Formal analysis. **Andrés Juan:** Writing – review & editing, Writing – original draft, Supervision, Resources, Methodology, Investigation. **Rosa Ieda L. V.:** Visualization, Formal analysis, Conceptualization.

Declaration of Competing Interest

The authors declare that they have no known competing financial interests or personal relationships that could have appeared to influence the work reported in this paper.

Data availability

Data will be made available on request.

Appendix A. Supporting information

Supplementary data associated with this article can be found in the online version at doi:10.1016/j.jallcom.2024.173525.

References

[1] M. Hojamberdiev, M.S. Bozgeyik, A.M. Abdullah, M.F. Bekheet, G. Zhu, Y. Yan, Y. Xu, K. Okada, Hydrothermal-induced growth of $Ca_{10}V_6O_{25}$ crystals with various morphologies in a strong basic medium at different temperatures, Mater. Res. Bull. 48 (2013) 1388–1396.

[2] L. Pei, Y. Pei, Y. Xie, C. Fan, D. Li, Q. Zhang, Formation process of calcium vanadate nanorods and their electrochemical sensing properties, J. Mater. Res. 27 (2012) 2391–2400.

[3] L.Z. Pei, Y.Q. Pei, Y.K. Xie, C.Z. Yuan, D.K. Li, Q.-F. Zhang, Growth of calcium vanadate nanorods, CrystEngComm 14 (2012) 4262.

[4] L. Li, S. Zheng, S. Wang, H. Du, Y. Zhang, Thermal hydrolysis synthesis and characterization of monoclinic metahewettite $CaV_6O_{16} \cdot 3H_2O$, J. Wuhan. Univ. Technol. -Mater. Sci. Ed. 29 (2014) 433–440.

[5] M.M. Teixeira, R.C. de Oliveira, M.C. Oliveira, R.A. Pontes Ribeiro, S.R. de Lazaro, M.S. Li, A.J. Chiquito, L. Gracia, J. Andres, E. Longo, Computational chemistry meets experiments for explaining the geometry, electronic structure, and optical properties of $Ca_{10}V_6O_{25}$, Inorg. Chem. 57 (2018) 15489–15499.

[6] M.M. Teixeira, Y.G. Gobato, L. Gracia, L.F. da Silva, W. Avansi, M. Assis, R.C. de Oliveira, G.A. Prando, J. Andrés, E. Longo, Towards a white-emitting phosphor $Ca_{10}V_6O_{25}$ based material, J. Lumin. 220 (2020) 116990.

[7] K. Qiu, J. Li, J. Li, X. Lu, Y. Gong, J. Li, Luminescence property of $Ca_3(VO_4)_2$:Eu^{3+} dependence on molar ratio of Ca/V and solution combustion synthesis temperature, J. Mater. Sci. 45 (2010) 5456–5462.

[8] C. Kumari, J. Manam, S.K. Sharma, Strong red emission in double perovskite Sr_3LiSbO_6:Eu^{3+} phosphor with high color purity for solid-state lighting applications, Mater. Sci. Semicond. Process. 158 (2023) 107385.

[9] M. Yang, J. Quan, Y. Zhou, L. Lin, W. Jiang, Z. Zhang, Z. Kong, H. Ni, P. Chen, Single-crystal structure, cation distribution, and optical/magnetic properties of Ce^{3+}-doped $Gd_3Al_2Ga_3O_{12}$ crystal, J. Cryst. Growth 621 (2023) 127380.

[10] I.M. Pinatti, I.C. Nogueira, W.S. Pereira, P.F. Pereira, R.F. Goncalves, J.A. Varela, E. Longo, I.L. Rosa, Structural and photoluminescence properties of Eu^{3+} doped a-Ag_2WO_4 synthesized by the green coprecipitation methodology, Dalton Trans. 44 (2015) 17673–17685.

[11] I.M. Pinatti, T.G. Ireland, G.R. Fern, I.L.V. Rosa, J. Silver, Low temperature micro Raman and laser induced upconversion and downconversion spectra of europium doped silver tungstate $Ag_{2-3x}Eu_xWO_4$ nanorods, J. Mater. Sci. Mater. Electron. 28 (2016) 7029–7035.

[12] P.B. Almeida, I.M. Pinatti, R.C. de Oliveira, M.M. Teixeira, C.C. Santos, T. R. Machado, E. Longo, I.L.V. Rosa, Structural, morphological and photoluminescence properties of β-Ag_2MoO_4 doped with Eu^{3+}, Chem. Pap. (2021).

[13] W. Costa Macedo, A. Germano Bispo Junior, K. de Oliveira Rocha, A.E. de Souza Albas, A.M. Pires, S. Rainho Teixeira, E. Longo, Photoluminescence of Eu^{3+}-doped $CaZrO_3$ red-emitting phosphors synthesized via microwave-assisted hydrothermal method, Mater. Today Commun. 24 (2020) 100966.

[14] C.R.R. Almeida, L.X. Lovisa, A.A.G. Santiago, M.S. Li, E. Longo, C.A. Paskocimas, F. V. Motta, M.R.D. Bomio, One-step synthesis of $CaMoO_4$:Eu^{3+} nanospheres by ultrasonic spray pyrolysis, J. Mater. Sci. Mater. Electron. 28 (2017) 16867–16879.

[15] R.F. Gonçalves, L.S. Cavalcante, I.C. Nogueira, E. Longo, M.J. Godinho, J. C. Sczancoski, V.R. Mastelaro, I.M. Pinatti, I.L.V. Rosa, A.P.A. Marques, Rietveld

refinement, cluster modelling, growth mechanism and photoluminescence properties of CaWO$_4$:Eu^{3+} microcrystals, CrystEngComm 17 (2015) 1654–1666.

[16] R.F. Gonçalves, M.J. Godinho, A.P.A. Marques, M.R.C. Santos, I.L.V. Rosa, E. Longo, M.S. Li, J.L.S. Sa, L.S. Cavalcante, Structure, morphology, and optical properties of (Ca$_{1-3x}$Eu$_{2x}$)WO$_4$ microcrystals, Electron. Mater. Lett. 11 (2015) 193–197.

[17] A.A.G. Santiago, N.F. Andrade Neto, E. Longo, C.A. Paskocimas, F.V. Motta, M.R. D. Bomio, Fast and continuous obtaining of Eu^{3+} doped CeO$_2$ microspheres by ultrasonic spray pyrolysis: characterization and photocatalytic activity, J. Mater. Sci. Mater. Electron. 30 (2019) 11508–11519.

[18] G.G. Nascimento, N.F. Andrade Neto, L.M.P. Garcia, M.S. Li, E. Longo, C. A. Paskocimas, M.R.D. Bomio, F.V. Motta, Effect of the Eu^{3+} (x = 0, 1, 2 and 3 mol %) doped Zn$_{2-x}$TiO$_4$ and Zn$_2$Ti$_{1-x}$O$_4$ obtained by complex polymerization method: photoluminescent and photocatalytic properties, J. Mater. Sci. Mater. Electron. 30 (2019) 20979–20988.

[19] L.X. Lovisa, J. Andrés, L. Gracia, M.S. Li, C.A. Paskocimas, M.R.D. Bomio, V. D. Araujo, E. Longo, F.V. Motta, Photoluminescent properties of ZrO$_2$: Tm^{3+}, Tb^{3+}, Eu^{3+} powders—a combined experimental and theoretical study, J. Alloy. Compd. 695 (2017) 3094–3103.

[20] R.F. Gonçalves, A.P. Moura, M.J. Godinho, E. Longo, M.A.C. Machado, D.A. de Castro, M. Siu Li, A.P.A. Marques, Crystal growth and photoluminescence of europium-doped strontium titanate prepared by a microwave hydrothermal method, Ceram. Int. 41 (2015) 3549–3554.

[21] T.M. Mazzo, I.M. Pinatti, L.R. Macario, W. Avansi, M.L. Moreira, I.L.V. Rosa, V. R. Mastelaro, J.A. Varela, E. Longo, Europium-doped calcium titanate: optical and structural evaluations, J. Alloy. Compd. 585 (2014) 154–162.

[22] T.M. Mazzo, L. Mendonça da Rocha Oliveira, L.R. Macario, W. Avansi, Rd Silveira André, I.L. Viana Rosa, J.A. Varela, E. Longo, Photoluminescence properties of CaTiO$_3$:Eu^{3+} nanophosphor obtained by the polymeric precursor method, Mater. Chem. Phys. 145 (2014) 141–150.

[23] M.M. Ferrer, Y.V. de Santana, C.W. Raubach, F.A. La Porta, A.F. Gouveia, E. Longo, J.R. Sambrano, Europium doped zinc sulfide: a correlation between experimental and theoretical calculations, J. Mol. Model. 20 (2014) 2375.

[24] F.V.D. Motta, A.P.D.A. Marques, V.D.D. Araújo, M.T.D.S. Tavares, M.R. B. Delmonte, C.A. Paskocimas, M.S. Li, R.M.D. Nascimento, E. Longo, Optical characterization of europium-doped indium hydroxide nanocubes obtained by microwave-assisted hydrothermal method, Mater. Res. 17 (2014) 933–939.

[25] R.S. André, E.C. Paris, M.F.C. Gurgel, I.L.V. Rosa, C.O. Paiva-Santos, M.S. Li, J. A. Varela, E. Longo, Structural evolution of Eu-doped hydroxyapatite nanorods monitored by photoluminescence emission, J. Alloy. Compd. 531 (2012) 50–54.

[26] P.F.S. Pereira, A.P. de Moura, I.C. Nogueira, M.V.S. Lima, E. Longo, P.C. de Sousa Filho, O.A. Serra, E.J. Nassar, I.L.V. Rosa, Study of the annealing temperature effect on the structural and luminescent properties of SrWO$_4$:Eu phosphors prepared by a non-hydrolytic sol–gel process, J. Alloy. Compd. 526 (2012) 11–21.

[27] A.P. Marques, M.T. Tanaka, E. Longo, E.R. Leite, I.L. Rosa, The role of the Eu3+ concentration on the SrMoO$_4$:Eu phosphor properties: synthesis, characterization and photophysical studies, J. Fluoresc. 21 (2011) 893–899.

[28] I.L. Rosa, A.P. Marques, M.T. Tanaka, F.V. Motta, J.A. Varela, E.R. Leite, E. Longo, Europium(III) concentration effect on the spectroscopic and photoluminescent properties of BaMoO$_4$:Eu, J. Fluoresc. 19 (2009) 495–500.

[29] A.P. de Moura, L.H. de Oliveira, E.C. Paris, M.S. Li, J. Andres, J.A. Varela, E. Longo, I.L. Rosa, Photolumiscent properties of nanorods and nanoplates Y$_2$O$_3$:Eu^{3+}, J. Fluoresc. 21 (2011) 1431–1438.

[30] D.P. Volanti, I.L.V. Rosa, E.C. Paris, C.A. Paskocimas, P.S. Pizani, J.A. Varela, E. Longo, The role of the Eu^{3+} ions in structure and photoluminescence properties of SrBi$_2$Nb$_2$O$_9$ powders, Opt. Mater. 31 (2009) 995–999.

[31] J. Gu, B. Yan, Hydrothermal synthesis and luminescent properties of Ca$_2$V$_2$O$_7$:Eu^{3+} phosphors, J. Alloy. Compd. 476 (2009) 619–623.

[32] R. Dovesi, V.R. Saunders, C. Roetti, R. Orlando, C.M. Zicovich-Wilson, F. Pascale, B. Civalleri, K. Doll, N.M. Harrison, I.J. Bush, P. D'Arco, M. Llunel, M. Causà, Y. Noël, L. Maschio, A. Erba, M. Rérat, S. Casassa, CRYSTAL17 User's Manual, University of Torino, 2017.

[33] M. Cattit, R. Dovesit, A. Paveses, V.R. Saunders, Elastic constants and electronic structure of fluorite (CaF$_2$): an ab initio Hartree-Fock study, J. Phys. Condens. Matter 3 (1991) 4151–4164.

[34] W.C. Mackrodt, N.M. Harrison, V.R. Saunders, N.L. Allan, M.D. Towler, E. Aprà, R. Dovesi, Ab initioHartree-Fock calculations of CaO, VO, MnO and NiO, Philos. Mag. A 68 (1993) 653–666.

[35] M. Corno, C. Busco, B. Civalleri, P. Ugliengo, Periodic ab initio study of structural and vibrational features of hexagonal hydroxyapatite Ca$_{10}$(PO$_4$)$_6$(OH)$_2$, Phys. Chem. Chem. Phys. PCCP 8 (2006) 2464–2472.

[36] H.A. Eick, N.C. Baenziger, L. Eyring, The preparation, crystal structure and some properties of SmN, EuN and YbN^1, J. Am. Chem. Soc. 78 (1956) 5987–5989.

[37] H.A. Eick, N.C. Baenziger, L. Eyring, Lower oxides of samarium and europium. the preparation and crystal structure of SmO$_{0.4-0.6}$, SmO and EuO^1, J. Am. Chem. Soc. 78 (1956) 5147–5149.

[38] L. Maschio, B. Kirtman, M. Rerat, R. Orlando, R. Dovesi, Ab initio analytical Raman intensities for periodic systems through a coupled perturbed Hartree-Fock/Kohn-Sham method in an atomic orbital basis. I. Theory, J. Chem. Phys. 139 (2013) 164101.

[39] L.S. Cavalcante, V.M. Longo, J.C. Sczancoski, M.A.P. Almeida, A.A. Batista, J. A. Varela, M.O. Orlandi, E. Longo, M.S. Li, Electronic structure, growth mechanism and photoluminescence of CaWO$_4$ crystals, CrystEngComm 14 (2012) 853–868.

[40] L.S. Cavalcante, M.A. Almeida, W. Avansi Jr., R.L. Tranquilin, E. Longo, N. C. Batista, V.R. Mastelaro, M.S. Li, Cluster coordination and photoluminescence properties of α-Ag$_2$WO$_4$ microcrystals, Inorg. Chem. 51 (2012) 10675–10687.

[41] A.G. Souza, O.P. Ferreira, E.J.G. Santos, J. Mendes, O.L. Alves, Raman spectra in vanadate nanotubes revisited, Nano Lett. 4 (2004) 2099–2104.

[42] D.R. Herschbach, V.W. Laurie, Anharmonic potential constants and their dependence upon bond length, J. Chem. Phys. 35 (1961) 458–464.

[43] A.A. Zavitsas, Factors affecting the relation between stretching frequencies and bond lengths. Diatomic and polyatomic species without adjustable fitting parameters, Spectrochim. Acta Part A Mol. Biomol. Spectrosc. 151 (2015) 553–565.

[44] M.A. Pogosova, F. Azarmi, A.A. Eliseev, P.E. Kazin, Eu and Cu co-substituted calcium vanadate — the crystal structure, luminescence and color, Dyes Pigments 148 (2018) 219–223.

[45] B. Philips-Invernizzi, Bibliographical review for reflectance of diffusing media, Opt. Eng. 40 (2001) 1082.

[46] D.L. Wood, J. Tauc, Weak absorption tails in amorphous semiconductors, Phys. Rev. B 5 (1972) 3144–3151.

[47] F. Urbach, The long-wavelength edge of photographic sensitivity and of the electronic absorption of solids, Phys. Rev. 92 (1953), 1324-1324.

[48] O.V. Chukova, S.G. Nedilko, A.A. Slepets, S.A. Nedilko, T.A. Voitenko, Synthesis and properties of the La$_{1-x-y}$Eu$_y$Ca$_x$VO$_4$ (0 </= x, y </= 0.2) compounds, Nanoscale Res. Lett. 12 (2017) 340.

[49] J. Huang, Q. Li, D. Chen, Preparation and luminescence properties of Ca$_3$(VO$_4$)$_2$: Eu^{3+}, Sm^{3+} phosphor for light-emitting diodes, Mater. Sci. Eng. B 172 (2010) 108–113.

[50] H. Kaur, M. Jayasimhadri, Color tunable photoluminescence properties in Eu^{3+} doped calcium bismuth vanadate phosphors for luminescent devices, Ceram. Int. 45 (2019) 15385–15393.

[51] H. Li, M. Fang, Z. Huang, Yg Liu, H. Zhu, X. Min, L. Zhang, Energy transfer mechanism and color-tunable luminescence properties of Eu^{3+}-doped BaMg$_2$V$_2$O$_8$ vanadate phosphors, Chem. Phys. Lett. 662 (2016) 86–90.

[52] Y. Li, N. Li, P. Zhang, Z. Wei, Z. Wang, L. Zhao, W. Chen, Deep-red photoluminescence from enhanced ^{5}D$_0$-^{7}F$_4$ transition in Eu^{3+} doped Ca$_2$Ga$_2$GeO$_7$ phosphors, Spectrochim. Acta Part A Mol. Biomol. Spectrosc. 248 (2021) 119247.

[53] K.N. Shinde, R. Singh, S.J. Dhoble, Photoluminescence characteristics of the single-host white-light-emitting Sr$_{3-3/2}$(VO$_4$)$_2$:xEu (0≤x≤0.3) phosphors for LEDs, J. Lumin. 146 (2014) 91–96.

[54] X. Mi, H. Shi, Z. Wang, L. Xie, H. Zhou, J. Su, J. Lin, Luminescence properties of M$_3$(VO$_4$)$_2$:Eu^{3+}(M = Ca, Sr, Ba) phosphors, J. Mater. Sci. 51 (2015) 3545–3554.

[55] N. Zhang, J. Li, J. Wang, R. Shi, L. Chen, A. Zhang, P. Yang, A vanadate-based white light emitting luminescent material for temperature sensing, RSC Adv. 9 (2019) 30045–30051.

[56] M. Toro-Gonzalez, R. Copping, S. Mirzadeh, J.V. Rojas, Multifunctional GdVO$_4$:Eu core-shell nanoparticles containing ^{225}Ac for targeted alpha therapy and molecular imaging, J. Mater. Chem. B 6 (2018) 7985–7997.